Fuel 352 (2023) 128847

Contents lists available at ScienceDirect

Fuel

journal homepage: www.elsevier.com/locate/fuel

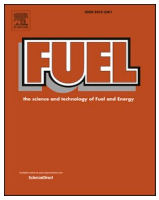

Full Length Article

Determination of the statistical distribution of drag and lift coefficients of refuse derived fuel by computer vision

Robin Streier [a,*], Siegmar Wirtz [a], Krasimir Aleksandrov [b], Hans-Joachim Gehrmann [b], Dieter Stapf [b], Miao Zhang [c], Markus Vogelbacher [c], Jörg Matthes [c], Viktor Scherer [a]

[a] Department of Energy Plant Technology, Ruhr-University Bochum, Universitätsstraße 150, 44780 Bochum, Germany
[b] Institute for Technical Chemistry, Karlsruhe Institute of Technology, Hermann-von-Helmholtz-Platz 1, 76344 Eggenstein-Leopoldshafen, Germany
[c] Institute for Automation and Applied Informatics, Karlsruhe Institute of Technology, Hermann-von-Helmholtz-Platz 1, 76344 Eggenstein-Leopoldshafen, Germany

ARTICLE INFO

Keywords:
Drag and lift coefficients
Refuse derived fuel
Computer vision
Photogrammetry
Stereo vision

ABSTRACT

This research investigates the flight behavior of refuse-derived fuel (RDF) in a drop shaft using Computer Vision to obtain statistical data on the aerodynamic properties of the particles.

Methods to determine 3D geometry models of complex-shaped particles by photogrammetry and to obtain time resolved particle positions and velocities are described. Furthermore, an approach to obtain the frequency distribution of drag and lift coefficients from photogrammetric analysis and drop shaft experiments is presented. The image evaluation is based on algorithms of the open-source libraries OpenCV, COLMAP as well as MeshLab and Open3D. The precision of the system is validated employing model particles with known geometry. The 3D particle models overestimate the particle surface area by 4.58 %, the position detection works with a mean deviation of 2.73 %. The average sink rate is calculated with an accuracy of 4.87 % and the drag coefficient with an accuracy of 2.08 %. Finally, the frequency distribution of four RDF fractions, namely, textiles, cardboard, 3D plastic particles and 2D plastic foils are presented.

1. Introduction

Cement production is an energy-intensive process and is responsible for 6 – 8 % of global anthropogenic CO_2 emissions [1]. Two-thirds are due to the release of CO_2 from calcination and one-third stems from combustion of fuels to provide the heat for the endothermic calcination and the clinker burning process. Fuels like coal, heating oil and refuse-derived fuels are used. Since the latter contains biogenic components, the fuel-related CO_2 emissions can be reduced with increasing substitution by refuse-derived fuels (RDF) [2]. The light fraction of pre-processed solid waste, so-called FLUFF, is used as RDF in cement rotary kilns, because it can be pneumatically conveyed into the combustion chamber similar as pulverized coal [3]. Compared to the current standard fuel, pulverized coal, the composition of FLUFF is heterogeneous as it contains different waste fractions like plastic foils, cardboard and paper. In addition, the FLUFF particles are of complex shape and have dimensions in the centimetre range, whereas pulverized coal shows particle sizes in the 100 μm range, i.e. the assumption of nearly spherical particles can be made for coal. For pulverized coal, the point mass assumption often used in CFD simulations is justified, this is not the case for FLUFF. FLUFF particles are not symmetrical and their geometric center can differ from the center of mass. Because of this and its irregular shape, rotation is initiated, which leads to complex trajectories [4,5]. In CFD codes, drag and lift coefficients and the relative velocity are used to calculate the fluid forces acting on a particle. For RDF, these coefficients are not single values, instead a frequency distribution of the coefficients will be present due to the heterogeneity of the particle properties. A method how these frequency distributions can be incorporated in CFD codes to predict the flight behaviour of RDF can be found, for example, in Liedmann et al. [3] and Pieper et al. [6]. To derive the respective drag and lift coefficients, the relative position, velocity, particle shape and projected area with respect to the velocity vector (hereafter referred to as flow area) of the particles are needed. The various steps for obtaining these parameters are described in this paper.

The literature concerning the flight behaviour of RDF is scarce. However, there are several studies dealing with the investigation of aerodynamic properties of non-spherical particles [7–9] using the sphericity as a simplified parameter to describe the influence of particle

* Corresponding author.
E-mail address: streier@leat.rub.de (R. Streier).

https://doi.org/10.1016/j.fuel.2023.128847
Received 22 February 2023; Received in revised form 5 May 2023; Accepted 28 May 2023

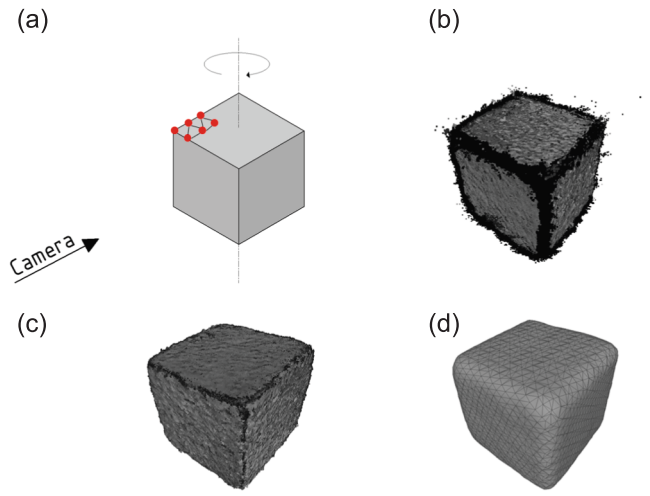

Fig. 1. Procedure to obtain a 3D model of an object. (a) Structure from Motion method. (b) raw point cloud. (c) revised point cloud: removal of black pixels and statistical outliers as well as reducing the number of voxels. (d) 3D model.

shape. Song et al. [10] developed a correlation for the drag coefficient of spherical and non-spherical particles (cubes and cylinders) including the effect of the particle sphericity and the particle settling orientation. Nakhaei et al. [11] proposed a method using the terminal velocity to estimate the mass distribution of RDF samples from a wind sieve. The terminal velocity was calculated using a 2D imaging setup to derive the maximum flow area. In [4], our group investigated the flight behavior of RDF particles with a camera based approach in a drop shaft. The particle geometry was estimated from two orthogonal projections of the particles, thus, overestimating the surface area and, hence, the flow area. Along the recorded particle tracks, the sequence of orientations was obtained in a simplified manner, employing intersecting lines. As both, geometry and change of orientation enter the calculation of lift and drag coefficients, this approach tends to predict too small values [12]. In addition, Krueger et al. [4] used a camera system with a frame rate of just 50 frames per second, which limits the temporal resolution of particle orientation.

This article is an extension and improvement of the work of Krueger et al. [4]. In the current article, an approach is presented which improves the determination of drag and lift coefficients by enhancing the time resolution of particle detection by a factor of 10 and applying a new computer vision based method to determine correct shape and orientation of the particles. For this purpose, photogrammetric investigations are combined with drop shaft experiments in order to properly determine the current flow area (which cannot be seen with a normal camera setup) along the trajectory.

2. Determination of the particle geometry and flight behavior

Detailed knowledge of the particle shape is essential to define the flow area. Flow area and relative velocity determine drag and lift coefficient, which govern the flight track evolution. The following sections provide an overview of the methods and the experimental setup to determine the flight characteristics of RDF.

2.1. Determination of the geometry of RDF particles

The “Structure from Motion” method is used to determine the particle geometry. It is a procedure, which uses characteristic points from several images taken by one camera from different viewpoints to create a 3D model of an object. It does not matter whether the camera moves around a fixed object or whether the object moves in front of a fixed camera [13]. Fig. 1a shows the principal procedure applied for a cube.

While the cube rotates around its own axis, a fixed camera captures images from different directions. Features (symbolized as red dots) are detected using the SIFT algorithm by David Lowe [14] to identify so-called keypoints. These keypoints arise from textures or edges of the object. By taking into account the pixels surrounding a keypoint, a numerical descriptor can be obtained to refer to the same keypoint in different images. A keypoint position in conjunction with its descriptor is denoted as a “feature”. The process requires an initial calibration of the camera using a checkerboard and Zhangś method to get the intrinsic parameters and distortion coefficients to subsequently undistort the captured images [15]. Then, the images obtained are converted into binary images utilizing a threshold operation to create a mask around the illuminated particle to detach it from the background. Features are only searched and detected inside this mask to not accidentally identify features from the field of view behind the particle.

Afterwards, features identified on different images are matched. Image pairs and their corresponding valid matches are then used for the following 3D reconstruction. This is performed as a sparse reconstruction in the first place, which uses the information obtained in the feature matching to determine the camera positions relative to the object for each image [16]. From this, the rotation and translation vectors are computed for each camera position. Subsequently, this information is used to convert the sparse point set into a dense point cloud. The latter, in contrast to the sparse reconstruction, uses depth maps from the stereo

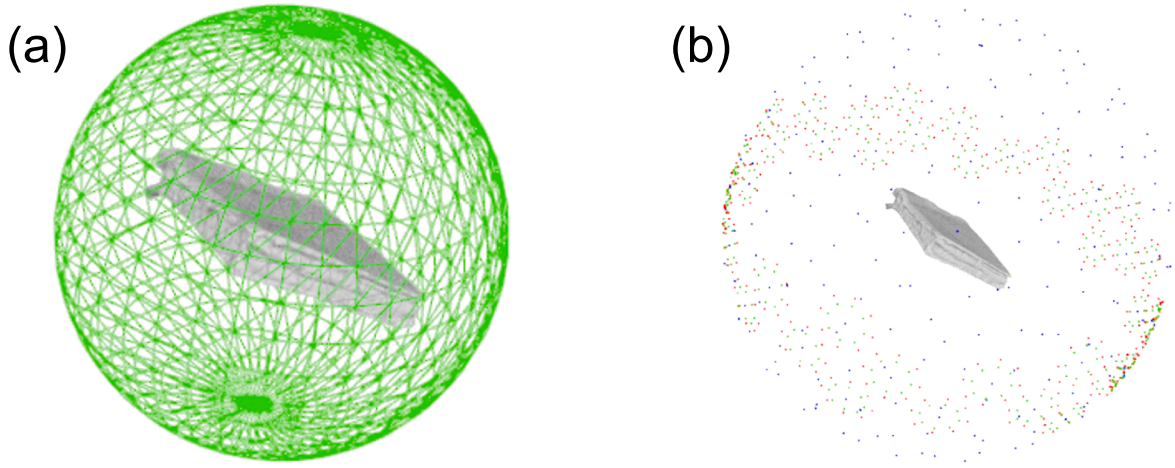

Fig. 2. Procedure to render images of the 3D model. (a) Sphere Creation. (b) Scene Positioning: Possible points to place a virtual camera pointing towards the center of the particle for recording images.

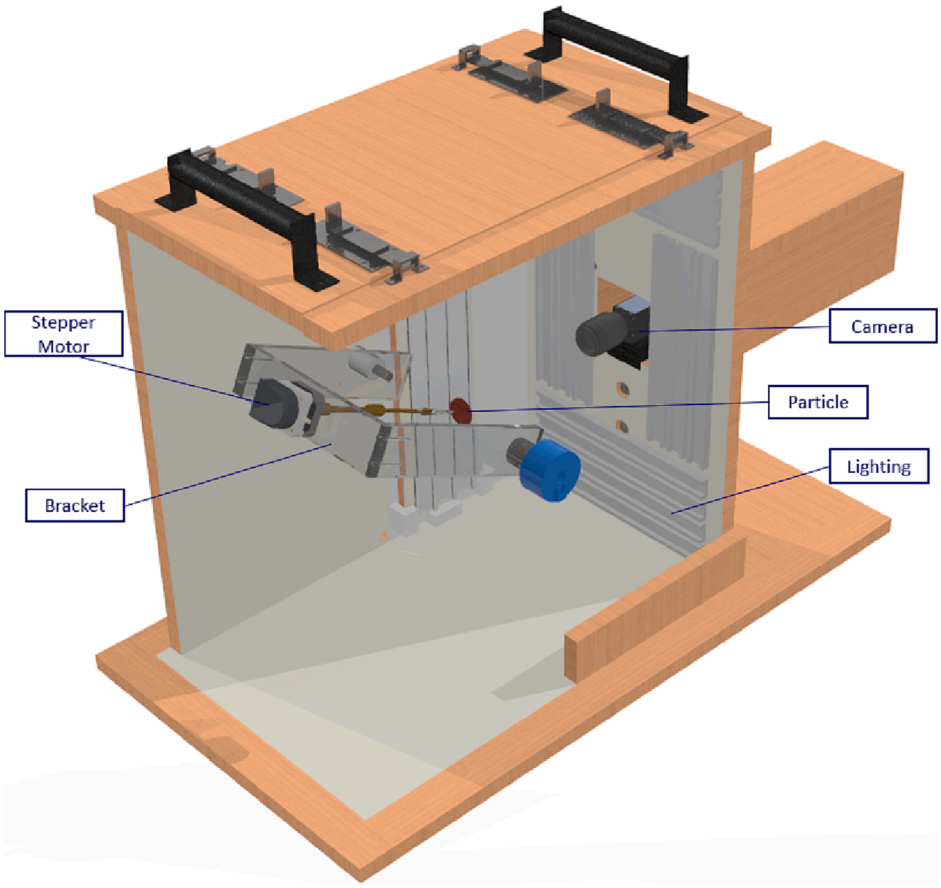

Fig. 3. Photogrammetry Station.

correspondences of the calculated camera positions to determine the surface texture of the object by computing the corresponding point normals and refining the surface points [13,16].

After the dense point cloud is created, some editing is necessary as not only features of the particle but also features of the particle mounting are localized. These undesired features and artefacts on the edges of the particle caused by the black background are removed as well as statistical outliers (see Fig. 1b and c). Moreover, a voxel mesh is used to uniformly resample the point cloud to create a new set with equally distributed points. The new point cloud preserves the original geometry, while the number of points is reduced, which accelerates surface reconstruction.

The latter is carried out either as a "Poisson Surface Reconstruction" for volumetric (3D objects) or as a "Ball Pivoting Algorithm" for flat objects like foils to generate a surface mesh connecting the features from the point cloud [17,18], as illustrated in Fig. 1d, producing a digital model of the original object.

To scale the mesh obtained to the actual size of the object, it is adjusted by a scaling factor. This value is obtained from the ratio between the length of a known reference polyhedron and the corresponding actual length of the reference object [13]. As a result, the geometrical model is stored, for instance in *.ply data format. Various geometric parameters (i.e. volume or inertia tensor) are calculated by integration over the polyhedron forming the object [19].

The algorithms used to obtain the 3D model are provided by OpenCV (camera calibration and threshold operation), COLMAP (point cloud creation), Open3D (editing of the dense point cloud) and MeshLab (mesh creation).

The digital model of the particle is required to define its geometry in a reference orientation. During flight tracking, the current orientation of the particle on each frame set must be determined. For this purpose, a Fibonacci sphere is created around the particle to obtain different discrete orientations of the previously created 3D model. The Fibonacci sphere provides a predefined number of almost equally distributed points on the surface. At these positions, a "virtual camera", pointing towards the center of the sphere, renders and records scenes of the particle model using Open3D (see Fig. 2 and [20,21] for more information; the red and green dots in Fig. 2b are additional points symbolizing virtual camera positions and visualized only around the equator for clarity). The rendered images are converted into binary images and stored for later comparison with the images of the actual particle along its track in the drop shaft, to obtain the particle orientation.

2.2. Photogrammetry Station

The visual appearance and shape of particles as well as their geometric properties are obtained with a photogrammetry station using the "Structure from Motion" method described above. The particle is fixed on a mounting, which is driven by a stepper motor to rotate around its own axis. The stepper motor, seen in Fig. 3, is installed on a bracket made of acrylic glass to improve the illumination inside the box. Another stepper motor outside the interior (not depicted in Fig. 3) drives the bracket additionally on another axis. This is done to capture many orientations of the particle for accurate 3D reconstruction. Capturing these images with a polarization camera (baumer VCXU-50 MP, 2448 × 2048 px) reduces reflections on the particle surface. The camera is equipped with a lens with a focal length of 35 mm. The distance from the camera to the particle can be flexibly adjusted depending on the particle size. The maximum particle size with the current system is 10 × 10 cm.

To create proper illumination, LED stripes (1,200 lm/m) are placed at the walls around the camera and on the wall to the right-hand side of it. Moreover, the inside walls are painted white to diffusively spread the

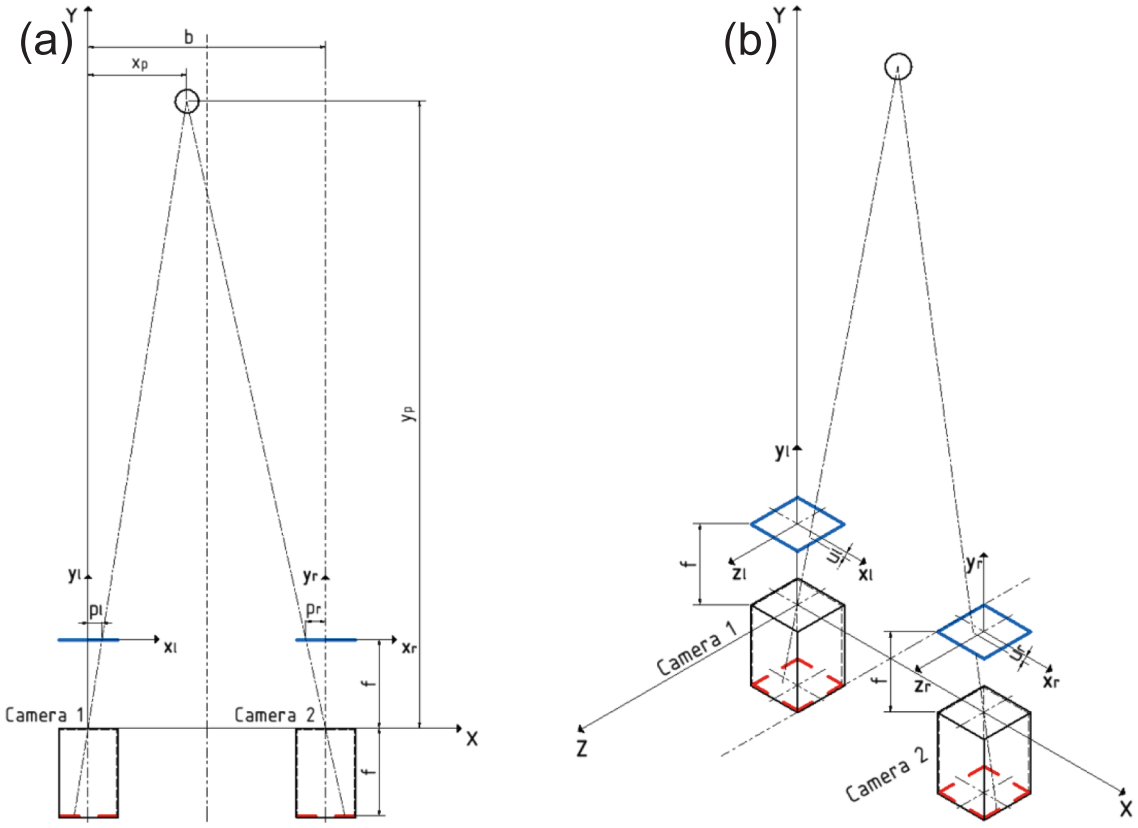

Fig. 4. Stereo Vision. (a) 2D view. (b) 3D view.

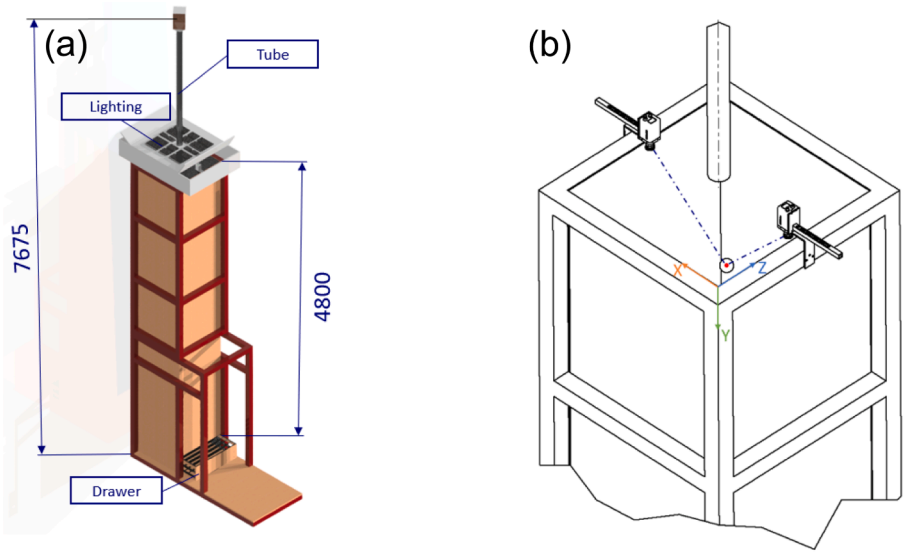

Fig. 5. Drop Shaft. (a) Dimensions and parts. (b) Camera setup and coordinate system.

light emitted by the LED modules to ensure a homogenous lighting. Only the wall opposite to the camera is painted black to achieve maximum contrast between the background and the illuminated particle. Approximately 180 images are needed to create a 3D model. The number of images taken by the camera can be set. Note that challenging particles (smooth surface, few features) need more images than structured particles (rough surface, many features). If more images are taken than necessary, it does not influence the final result, as only pairs of images with the most matching features are used to create the 3D model. As long as more than 500 features are detected per image, which is the case for the current study, the algorithm works reliably. More features can be made visible by adjusting the camera's exposure time or the colour of the emitted light (red, green, blue, white).

2.3. *Determination of the flight behavior*

Stereo vision is applied to determine flight behaviour. Stereo vision requires two cameras to determine depth (see Fig. 4) from differences in

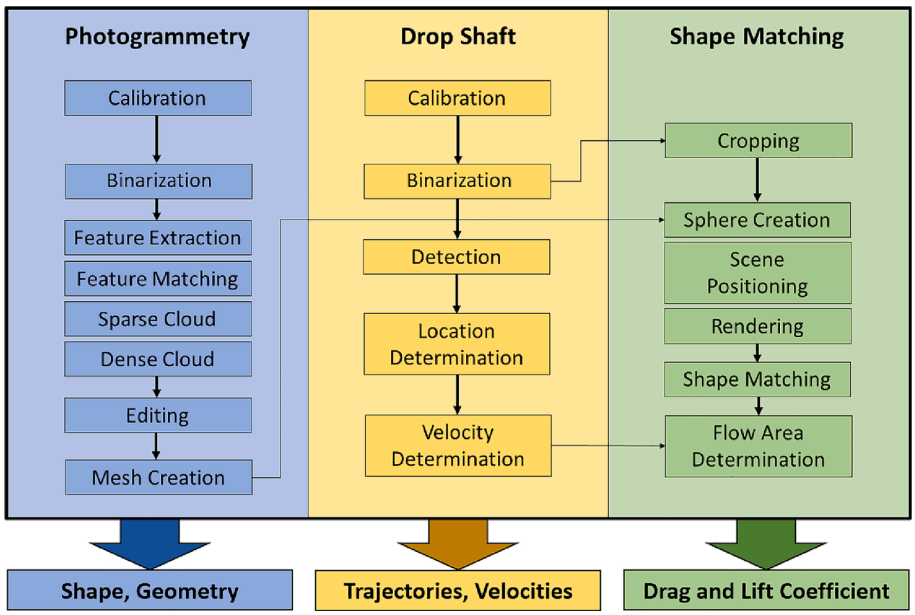

Fig. 6. Procedure for determining the aerodynamic properties.

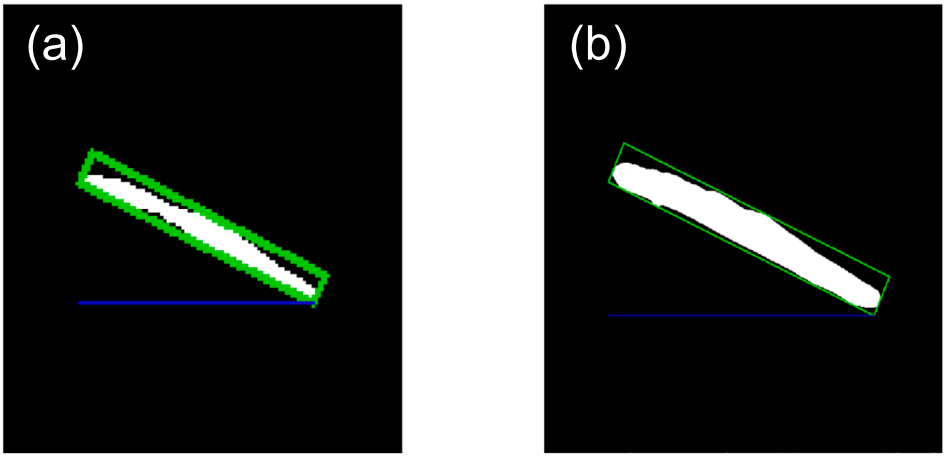

Fig. 7. Shape Matching. (a) Cropped image from the Drop Shaft (b) Cropped image from Scene Positioning.

the images. The general principle for a stereo pair within the x- and y-plane is depicted in Fig. 4a. The origin of the coordinate system has been placed in the optical center of camera 1. To calculate the distances x_p and y_p of the cameras to the object, the distance b between the cameras and the focal length f of the cameras have to be known [22]. The object is represented by a corresponding pixel on the sensor planes (symbolized in red) of the cameras. The light rays hitting the sensor create an inverted image of the object. The camera converts the images and displays them correctly in the image plane (symbolized in blue) [23].

The distance between the corresponding pixel and the optical center of the camera is given by p_l and p_r, which can be calculated by Equations (1) and (2) according to the theorem of intersecting lines. Note that the sign of the value of p_l and p_r depends on the position on the sensor with respect to the local camera coordinate system (see the axes y_l / x_l and y_r / x_r respectively).

$$p_l = \frac{x_p}{y_p} \cdot f \tag{1}$$

$$p_r = \frac{b - x_p}{y_p} \cdot f \tag{2}$$

The disparity d is defined in Equation (3).

$$d = p_l - p_r \tag{3}$$

The distance y_p, which provides information about the depth, is obtained from Equation (4) using Equation (1) and (2).

$$y_p = \frac{b \cdot f}{d} \tag{4}$$

By knowing the depth, the distance x_p as well as z_p (see Fig. 4a and b; for clarity, z_p is not shown in Fig. 4b) are calculated using Equations (5) and (6). Here, z_p is calculated in the same manner as x_p by forming the ratio between the object coordinate (x_p respectively z_p) and the pixel coordinate (p_l respectively u_l) and equating it with the ratio between the depth y_p and the focal length f.

$$x_p = \frac{y_p}{f} \cdot p_l \tag{5}$$

$$z_p = \frac{y_p}{f} \cdot u_l \tag{6}$$

The position of the object within successive frames, derived from Equations (4) to (6), is used to calculate the velocity in the spatial

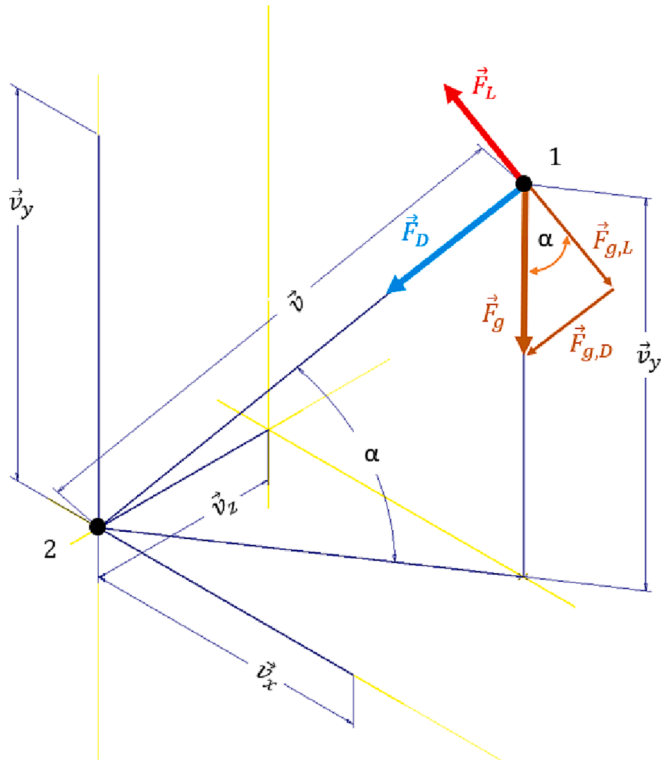

Fig. 8. Force equilibrium.

directions. For this purpose, the positional data of the current frame is compared with the next frame and multiplied by the frame rate of the cameras to calculate the velocity of the object by detecting the difference in particle position in subsequent images (Particle Tracking Velocimetry, PTV). The letter *n* denotes the current frame index and *c* stands for the framerate (fps, see Equation (7)) [24].

$$\vec{v} = \begin{pmatrix} {y_p}^{n+1} - {y_p}^{n} \\ {x_p}^{n+1} - {x_p}^{n} \\ {z_p}^{n+1} - {z_p}^{n} \end{pmatrix} \cdot c \tag{7}$$

Each camera is calibrated with a checkerboard image [15] before a measurement series. Moreover, a stereo calibration and stereo rectification based on epipolar geometries (see [25,26] for more information) is performed, which mathematically aligns the images captured by both cameras to provide accurate depth measurement. The images captured by the two cameras are converted into binary images to calculate the geometric center of the particle (see [27] for more information).

2.4. Drop Shaft

A drop shaft is used to analyze the statistics of the aerodynamic properties of an ensemble of RDF particles (in this case FLUFF). For this purpose, single particles (after their characterization in the photogrammetric station and weighing) are transported to the upper part of the drop shaft via a conveyor belt (not shown in Fig. 5a) and then fall through a tube into the interior of the drop shaft. Here, the trajectories of the particles are captured, as explained above, by two stereoscopically arranged cameras. The air in the drop shaft is quiescent.

The extra distance provided by the tube allows for acceleration of the particles to their terminal velocity before they are recorded by the cameras. The walls of the drop shaft are painted black to obtain a high contrast between the illuminated particle and the background. The lighting system consist of 18 LED modules providing a total luminous flux of 104,400 lm and is located at the top inlet of the drop shaft. Furthermore, a drawer with tilted panels is installed at the bottom of the drop shaft. When a particle hits the drawer, it is guided along the panels into the inside of the drawer and is afterwards no longer visible for the cameras. This is important to ensure that only one particle at a time is captured by the cameras as it passes through the drop shaft. The total distance between the top edge of the drawer and the location of the cameras is 4.8 m, the cross-sectional area inside the drop shaft is 0.83 m $\times$ 0.83 m.

The two high-speed cameras (baumer VLXT-28 M.I, 500 fps and 1920 $\times$ 1080 px) are used for image recording. Both cameras are aligned using overlapping x-axes and have the same position with respect to their z-axis and y-axis. The latter is aligned in such a way that the location of the entrance pupil of the two identical lenses (f = 4.8 mm) lies within the plane spanned by the upper edges of the drop shaft frame (see Fig. 5b). The entrance pupil is used as a reference for distance measurements for lenses with an aperture (see the pinhole model illustrated in Fig. 4 and [28] for further information). For typical RDF particles in the cm range and corresponding terminal velocities, no limitation concerning velocity are given due to the small exposure time of the cameras (1 ms). Only highly transparent (not coloured or not polluted foils) or extremely dark particles are challenging, because the reflection is partly missing, which leads to inaccuracies in the detection of the particles.

Fig. 9. 3D models of FLUFF particles. (a) plastics: 3D plastic particle (b) foils: 2D plastic foil.

Table 1
Accuracy of the computed geometric properties.

	3D Model	Actual Cube	Deviation [%]
Surface Area [10^{-6} m2]	2290. 09	2400	4.58
Inertia tensor [10^{-9} kg · m^2]	$\begin{pmatrix} 16.84 & 0 & 0 \\ 0 & 17.12 & 0 \\ 0 & 0 & 17.12 \end{pmatrix}$	$\begin{pmatrix} 16.33 & 0 & 0 \\ 0 & 16.33 & 0 \\ 0 & 0 & 16.33 \end{pmatrix}$	3.03 – 4.61

3. Procedure for determining the aerodynamic properties

After entering the drop shaft, the particle trajectory is recorded. Depending on mass and geometry of the particles, these tracks can vary considerably. Even a repetition of an experiment with the same particle will show a natural stochastic variation. To obtain the frequency distribution of the drag and lift coefficients along the tracks, the positions, orientations, velocities and the associated flow areas must be derived from the stereoscopic image sequences. An outline of the procedure is given in Fig. 6.

The output data of the photogrammetric investigations and drop shaft experiments are combined in a Shape Matching step. For this purpose, the binarized images are cropped and compared with the images rendered from the 3D model utilizing OpenCV.

Before the Shape Matching starts, the images rendered during Scene Positioning are cropped to the same ratio (size of the particle compared to size of the background) as the drop shaft images. The cropped images from Scene Positioning are additionally blurred. This procedure ensures nearly the same quality of the images to support Shape Matching. The latter is performed using the Hu moments (see [29] for more information). However, since the orientation obtained from the Hu moments is not always unique (if you for instance consider a cubicle or other symmetric objects), the algorithm is extended by an additional verification step, in which the orientation of the particles in one of the stereo images is compared to the orientation in the rendered images from Scene Positioning. In this verification, two piece of information are determined. The first is obtained by forming an aligned rectangle around the particle (see Fig. 7). Then, a horizontal line is created between the lowest and leftmost pixel (when the object is tilted to the left side) or the lowest and rightmost pixel (when the object is tilted to right side) of the rectangle. The angle spanned between this line and the rectangle characterises the particle orientation. The information whether the angle is spanned by the short or long side of the rectangle is the second piece of information employed. For example, the angle of the object in the drop shaft image may be the same as in the rendered image, but the object in the rendered image can be oriented vertically, while the object in the drop shaft image has a horizontal orientation. If the distance obtained from the Hu moment comparison multiplied by the difference of the calculated angles (requiring the same edges for the angle determination - “short” or “long” edge of the rectangle) is as small as possible and not negative, the shape and orientation are considered matched. Note that only drop shaft images with one outer contour (more can occur due to shading) are selected to avoid incorrect matching. Knowing the orientation of the rendered images from Scene Positioning, the flow area is determined. This is done by projecting the direction of the velocity vector (derived from the drop shaft experiments) onto the current orientation of the particle within the Scene Positioning. The value of the flow area A_{flow} is calculated in the following manner: the white counted pixels of the flow area n_{flow} are put into the ratio of a known reference number of white pixels $n_{white,\ ref}$ derived from the photogrammetric analysis and multiplied by the corresponding known area A_{ref} of a reference object [30] (see Equation (8)). With this method, the flow area, which basically is not visible with the drop shaft cameras from above, is obtained.

$$A_{flow} = \frac{A_{ref}}{n_{white,ref}} \cdot n_{white,flow} \tag{8}$$

Because of the high temporal resolution of the camera system, the velocity between two consecutive points (1 → 2) is assumed to stay constant (see Fig. 8). Therefore a balance of forces applies between the drag force F_D, the lift force F_L and the gravity force F_G, assuming that F_L lies in the same plane as F_D.

Knowing the velocity components v_y, v_x, v_z from the drop shaft investigation, the angle of attack α is calculated using Equation (9) to discriminate between the drag and lift forces (see Equations (10) and (11)).

$$\alpha = \arcsin\left(\frac{\left|\vec{v}_y\right|}{|\vec{v}|}\right) \tag{9}$$

$$\left|\vec{F}_D\right| = m_{particle} \cdot g \cdot \sin(\alpha) \tag{10}$$

$$\left|\vec{F}_L\right| = m_{particle} \cdot g \cdot \cos(\alpha) \tag{11}$$

From the velocity and flow area, the coefficients of drag and lift can be calculated according to [5] (see Equations (12) and (13)). Note that statistical outliers are removed using the quartile method [31].

$$c_D = \frac{2 \cdot \left|\vec{F}_D\right|}{\rho_{air} \cdot |\vec{v}|^2 \cdot A_{flow}} \tag{12}$$

$$c_L = \frac{2 \cdot \left|\vec{F}_L\right|}{\rho_{air} \cdot \overrightarrow{|\vec{v}|}^2 \cdot A_{flow}} \tag{13}$$

4. Results

4.1. Assessment of the accuracy of the system

Fig. 9 show examples of the 3D models derived from two of the FLUFF particles. Photos of these particles are shown in Fig. 13. Obviously, particle shape is represented with high spatial resolution.

Based on these 3D models, the surface area and the inertial tensor are determined. Table 1 serves as an example to show the mentioned parameters using a 3D model of a cube. By comparing geometric properties of the cube (side length of 20 mm and mass of 0.245 g) with the ones derived from the 3D model, the accuracy of the system is evaluated. The deviation of the surface area of the 3D model from the real geometry is less than 5 %.

For a proper estimation of the drag and lift coefficient, an accurate measurement of particle position is required. To verify this, a white Styrofoam ball is attached to a thread of varying length. Then the Styrofoam ball is placed at different distances from the cameras. Table 2 shows the camera-measured position of the non-moving Styrofoam ball, with a diameter of 30 mm, in y-direction. Note that the intersection of the field of view of the two cameras is at about 500 mm, so the position measurement starts at 600 mm and above. The position is determined up to a distance of 4.0 m with an average deviation of 2.73 %. As expected, particle detection deteriorates with increasing distance from the cameras.

In a next step, the results for the vertical velocitiy v_y are discussed (styrofoam ball). Depending on the shape and mass, some particles are not completely accelerated to their terminal velocity when entering the drop shaft. In case of the styrofoam ball, the ball enters the drop shaft nearly with its terminal velocity (see the increase in the velocity around

Table 2
Accuracy of the particle detection.

Thread length with Styrofoam ball [mm]	Drop Shaft Detection [mm]	Deviation [%]
600	595.065	0.82
900	883.04	1.88
1200	1170.51	2.46
1500	1459.13	2.72
1800	1746.17	2.99
2100	2048.4	2.46
3000	2878.83	4.04
4000	3821.27	4.47
Mean Deviation		2.73

0.5 m in Fig. 10). For the further trajectory, neglecting effects of vortex shedding, the assumption of a constant vertical velocity in the drop shaft is valid. However, Fig. 10 shows a fluctuation in velocity that becomes more pronounced when the distance to the cameras increases. This is due to the fact that position measurement gets worse with larger distances to the camera as discussed above. Since two particle positions enter the calculation of the particle velocity (see Equation (7), the uncertainty in determination of the particle velocity is larger compared to the position measurement. However, the range up to approximately 2 m shows the smallest fluctuations respectively uncertainties in the velocity measurement (see Fig. 10). Therefore, the velocity up to a distance of 2 m from the cameras is used for the evaluation to ensure a reliable determination of the drag and lift coefficients.

The accuracy of the velocity measurement is checked by averaging the velocity values shown in Fig. 10 and comparing them to the theoretical terminal velocity of the Styrofoam ball. As already said, it is assumed that the Styrofoam ball enters the drop shaft with its terminal velocity (thus eliminating the inertial force from the consideration). Due to the assumption of uniform flow around it, there is no dynamic lift force and the static lift force is neglected. Therefore, just the balance between the drag force and gravitational force of the Styrofoam ball remains. The calculated velocity of the ball is compared with the actually measured average velocity (see Table 3). The parameters used for the calculation can be found in Table 3 (where m stands for mass, d for diameter, ρ for density and c_D for the drag coefficient).

4.2. Drag coefficient for model particles

Spheres, cylinders and cubes have been selected as model particles and are used to compare the drag coefficients with literature data. For brevity, we concentrate on the drag coefficients, although lift coefficients have been determined as well. For example, the evaluated lift coefficient for spheres is zero, as expected.

As a first example of the results, Fig. 11 shows the evolution of the measured drag coefficient of a sphere along the particle trajectory in the drop shaft. The averaged value of the drag coefficient is 0.48 resulting in a deviation of 2.08 % from the literature value of 0.47 [32].

Fig. 12 gives an overview of the drag coefficients determined and their statistical deviation around the mean value in a box plot for spheres, cylinders and cubes. The boxes are spanned between the upper and lower quartiles of the data, with the median being the horizontal line in the middle of the box. The reliable data are within the range covered by the whiskers, anything outside this range is considered an outlier. For each particle geometry, 10 repetitions of the measurement including all datapoints during the flight sequence (greater than 100 datapoints for one model particle, $Re > 10^4$) have been performed. For spheres, the scatter around the mean value is small, as expected. The scatter for cylinders and cubes becomes naturally larger, as the orientation of these particles changes along their trajectory (they rotate).

Nevertheless, the mean values of the drag coefficient are in reasonable agreement with literature. For cubes, values of $c_D = 0.80$ ($10^4 < Re < 10^6$) for diagonal flow and $c_D = 1.05$ (for $10^4 < Re < 10^6$) for transverse flow are given in the literature [32]. For cylinders, the literature values are $c_D = 0.82$ for a longitudinal flow and $c_D = 1.2$ for transverse flow ($Re \approx 10^4$) [33,34]. Note that the literature values were measured, as mentioned, just for two particle-velocity orientations and do not take into account the influence of orientation and rotation in three dimensions on the drag coefficient [35]. In addition, the scatter is affected by the uncertainties in the determination of the velocity and flow area.

4.3. Drag and lift coefficients for RDF particles

As examples for FLUFF fractions textiles, cardboard, 3D plastic particles (denoted as plastics) and 2D plastic foils (denoted as foils) are considered. These are also the main fractions occurring in industrial FLUFF [12]. The particles stem from a sorting analysis of real FLUFF. Fig. 13 shows the typical appearance and dimensions of the particles with their average mass. The following results are based on a sample of 50 particles per fraction.

The averaged vertical velocity of the different FLUFF fractions is depicted in Fig. 14. 3D plastic and cardboard particles have the highest velocity because their mass is comparably large but with drag coefficients in the same order of magnitude as the other FLUFF fractions

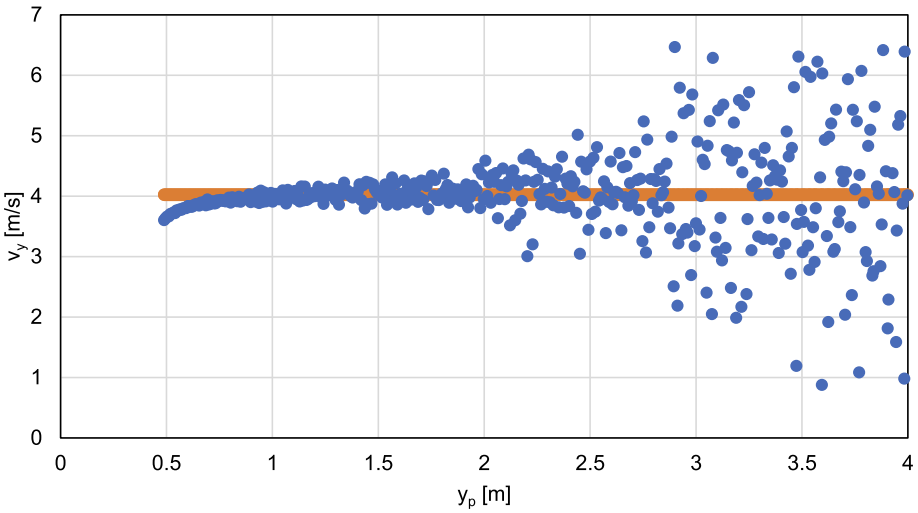

Fig. 10. Vertical velocity of a Styrofoam ball.

Table 3
Accuracy of the velocity measurement.

Case	Velocities [m/s]	Used Parameters
Theoretically calculated	3.84	$m_{sphere} = 0.3$ g $d_{sphere} = 30$ mm
Measured mean value	4.02	ρ_{air} (20 °C, 101,3 kPa) $= 1.204$ kg/m^3 $c_{D,\ sphere}$ ($10^3 < Re < 210^5$) $= 0.47$ [32]
Mean Deviation [%]	4.78	

(see Fig. 15).

Note that plastic particles tend to rotate because they are usually asymmetrical and have an irregular mass distribution over the particle. In the case of foils, the influence of rotation is not as dramatic, the flexibility of the particle results in a more "swinging motion" along their trajectory. The influence can be seen in the averaged drag and lift coefficients (see Figs. 15 and 16) and in the frequency distribution derived from all datapoints for the particles within the corresponding fraction (see Fig. 17), where plastic particles have the largest and foils the smallest drag coefficient. Vice versa, foils exhibit the highest lift coefficient and 3D plastics the smallest of all FLUFF fractions considered.

5. Conclusion and outlook

The current paper presents an improved method to study the flight characteristics of RDF particles to derive the frequency distribution of drag and lift coefficients of representative RDF fractions.

The measurement method is based on a detailed 3D geometry detection of the complex-shaped particles by photogrammetry as the geometry is the basic information to calculate the reference areas for the determination of drag and lift coefficients. The drag and lift coefficients are determined in a drop shaft, where the trajectories of individual particles are recorded by a stereoscopic high-speed (500 fps) camera system. The stereoscopic approach allows for the detection of particle position (and velocity by Particle Tracking Velocimetry) and

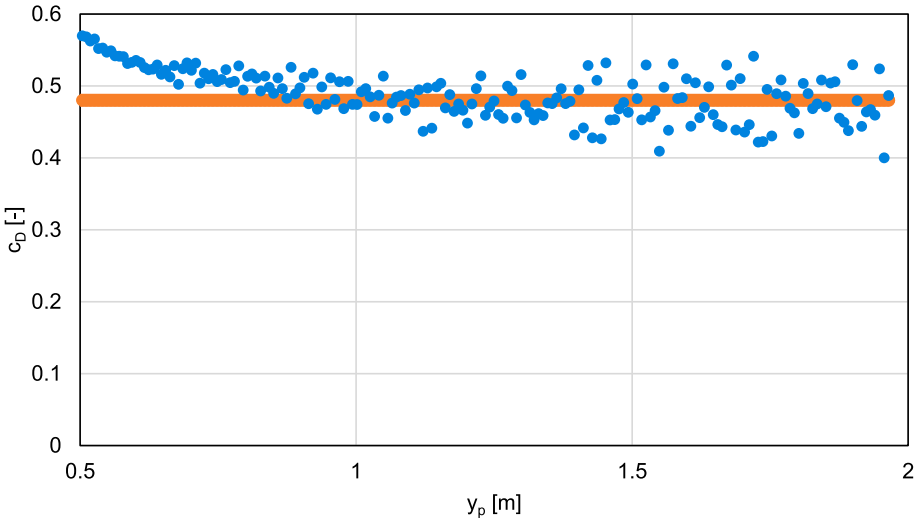

Fig. 11. Calculated drag coefficient for a sphere using the measured velocities and the Shape Matching approach.

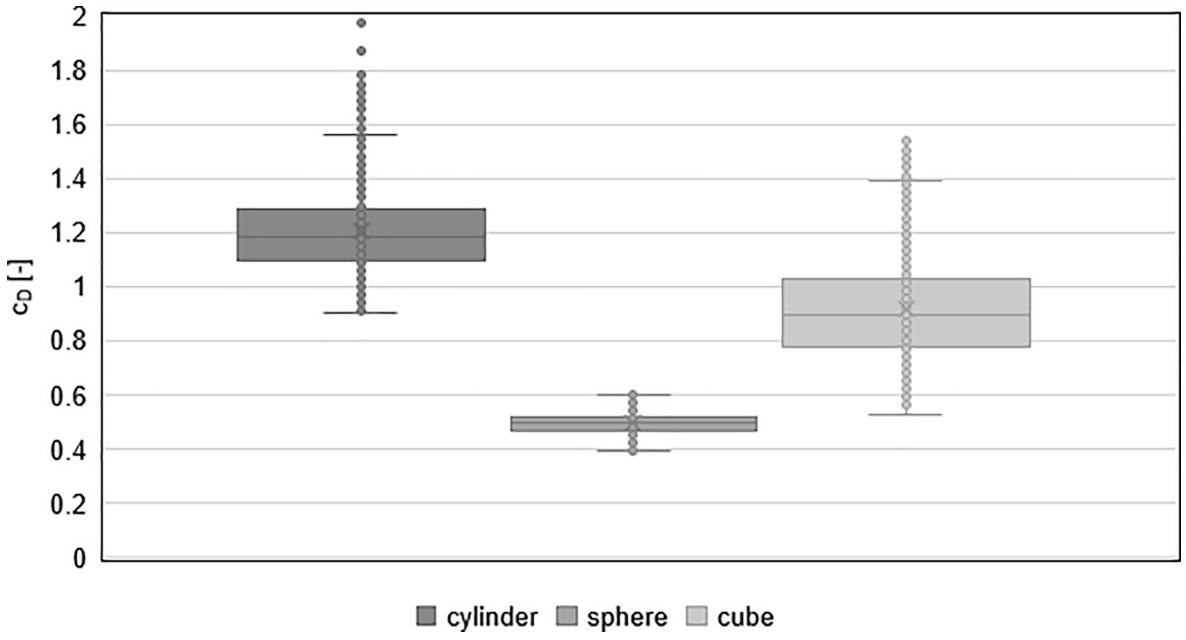

Fig. 12. Accuracy of calculated drag coefficients for model particles and the corresponding literature values represented as dashed lines.

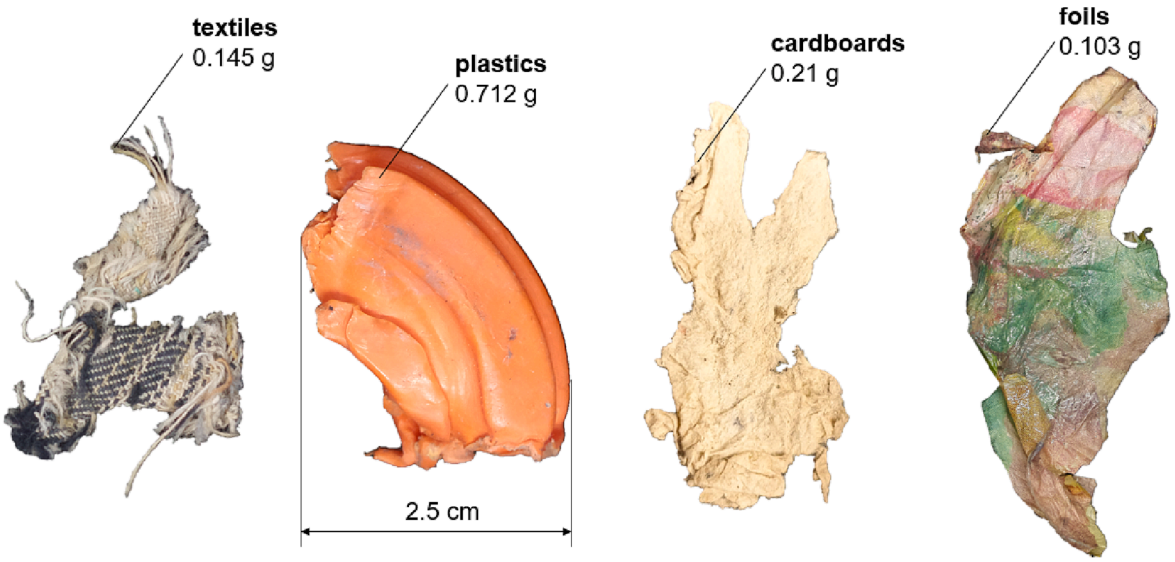

Fig. 13. Typical appearance of FLUFF particles with their average mass.

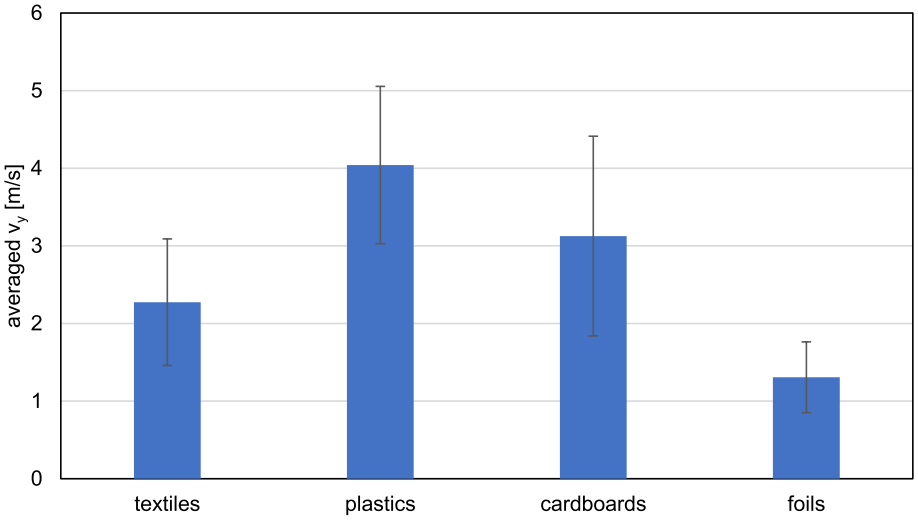

Fig. 14. Averaged vertical velocity and its standard deviation for the FLUFF fractions considered.

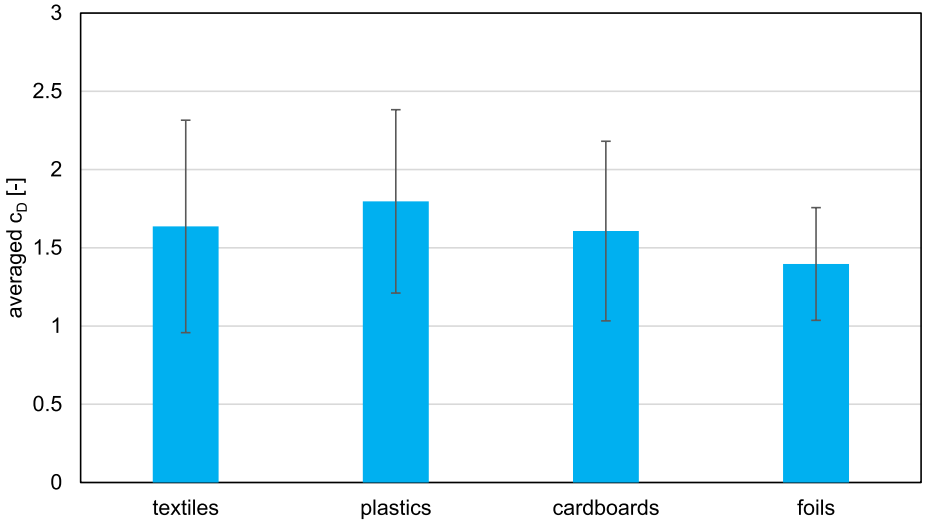

Fig. 15. Averaged drag coefficients and its standard deviation for the FLUFF fractions considered.

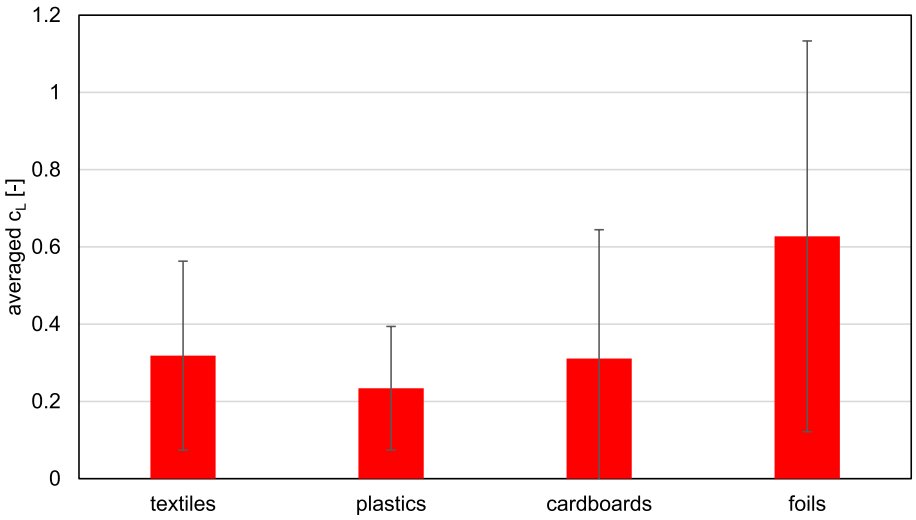

Fig. 16. Averaged lift coefficients and its standard deviation for the FLUFF fractions considered.

orientation. This information together with the knowledge of particle shape is used in an evaluation algorithm, described in detail, to derive drag and lift coefficients. By the measurement of multiple particles, the frequency distribution of the drag and lift coefficients for individual RDF fractions can be determined.

The accuracy of the system is checked using model particles (cubes, spheres, cylinders). In a first step, the accuracy of 3D shape reconstruction by photogrammetry is assed, showing that the surface area of a cube is adequately reproduced with a deviation below 5 %. Also the tensor of inertia is reproduced with good accuracy. As second step, a spherical particle is used to check the accuracy of the detection of particle position and velocity. The particle detection is reproduced with an average deviation of less than 3 %. The accuracy deteriorates with increasing distance of the particle from the cameras used for particle detection. This is mainly because the calculation of the geometric center becomes more inaccurate due to the smaller particle image on the camera sensor. This is also valid for the predicted sphere velocity, but deviation is less than 5 % compared to the calculated terminal velocity based on a simplified force balance. Third, the drag and lift coefficients of cubes, spheres, cylinders were determined. The drag coefficient of a sphere is calculated with a deviation less than 3 % from the literature value, which shows the reliability of the system. The values for the drag and lift coefficients lie well in the parameter range given by literature.

Finally, the averaged terminal velocity and frequency distributions of drag and lift coefficients for four different RDF fractions (textiles, plastic particles with 3D geometry, cardboards and 2D plastic foils) were measured. For each fraction, 50 individual particles were examined.

The averaged terminal velocities of Krueger et al. [5] agree well with the data obtained, as the terminal velocity for 3D plastic particles is also in the range of 4 m/s, for foils around 1.5 m/s and for cardboards around 3 m/s. This also matches the results of Nkhaei et al. [11] who observed that the average terminal velocity is larger than 3 m/s for plastics and cardboards and lower for foils.

For all fractions, the drag coefficients are significantly larger than lift coefficients. The maximum drag coefficient occurs for the 3D plastic particles. The mean value of the drag coefficients for the fractions spans from 1.4 to 1.7. The flat plastic foils show the largest average lift coefficient with a value of 0.6, whereas the 3D plastic particles exhibit the smallest value of around 0.2. The determined drag coefficients are larger than those derived by Krueger. This is in good agreement with the measurements carried out by Liedmann [12], who compared the particle geometry derived by the Krueger method with manual measurements. It was found that the Krueger method leads to an overestimation of the dimensions of the particle, resulting in too low values for the drag and lift coefficient. Larger drag coefficients as determined in the current study will have an influence of particle trajectories in corresponding CFD simulations. For the main application considered here, rotary cement kilns, the main parameter of interest is the axial penetration depth of the particles which is mainly influenced by the drag coefficient. Larger drag coefficient will reduce the penetration depth and may lead to an earlier impact of unburnt RDF particle onto the clinker bed, which can harm clinker quality due to locally reducing conditions in the clinker bed (oxygen for the conversion of RDF can be extracted from the mineralogical matrix).

In summary, the results obtained (frequency distribution of drag and lift coefficients as well as the inertia tensors) can be used to model the flight behavior of RDF particles in CFD simulations. In future work, we will extend an already existing approach of our group for the modelling of the flight and combustion behavior of RDF [3] with these information.

CRediT authorship contribution statement

Robin Streier: Investigation, Methodology, Software, Validation, Visualization, Writing – original draft, Writing – review & editing. **Siegmar Wirtz:** Conceptualization, Project administration, Supervision, Writing – review & editing. **Krasimir Aleksandrov:** Writing – review & editing. **Hans-Joachim Gehrmann:** Writing – review & editing. **Dieter Stapf:** Writing – review & editing. **Miao Zhang:** Writing – review & editing. **Markus Vogelbacher:** Writing – review & editing. **Jörg Matthes:** Writing – review & editing. **Viktor Scherer:** Supervision, Writing – review & editing, Conceptualization, Project administration.

Declaration of Competing Interest

The authors declare that they have no known competing financial interests or personal relationships that could have appeared to influence the work reported in this paper.

Data availability

Data will be made available on request.

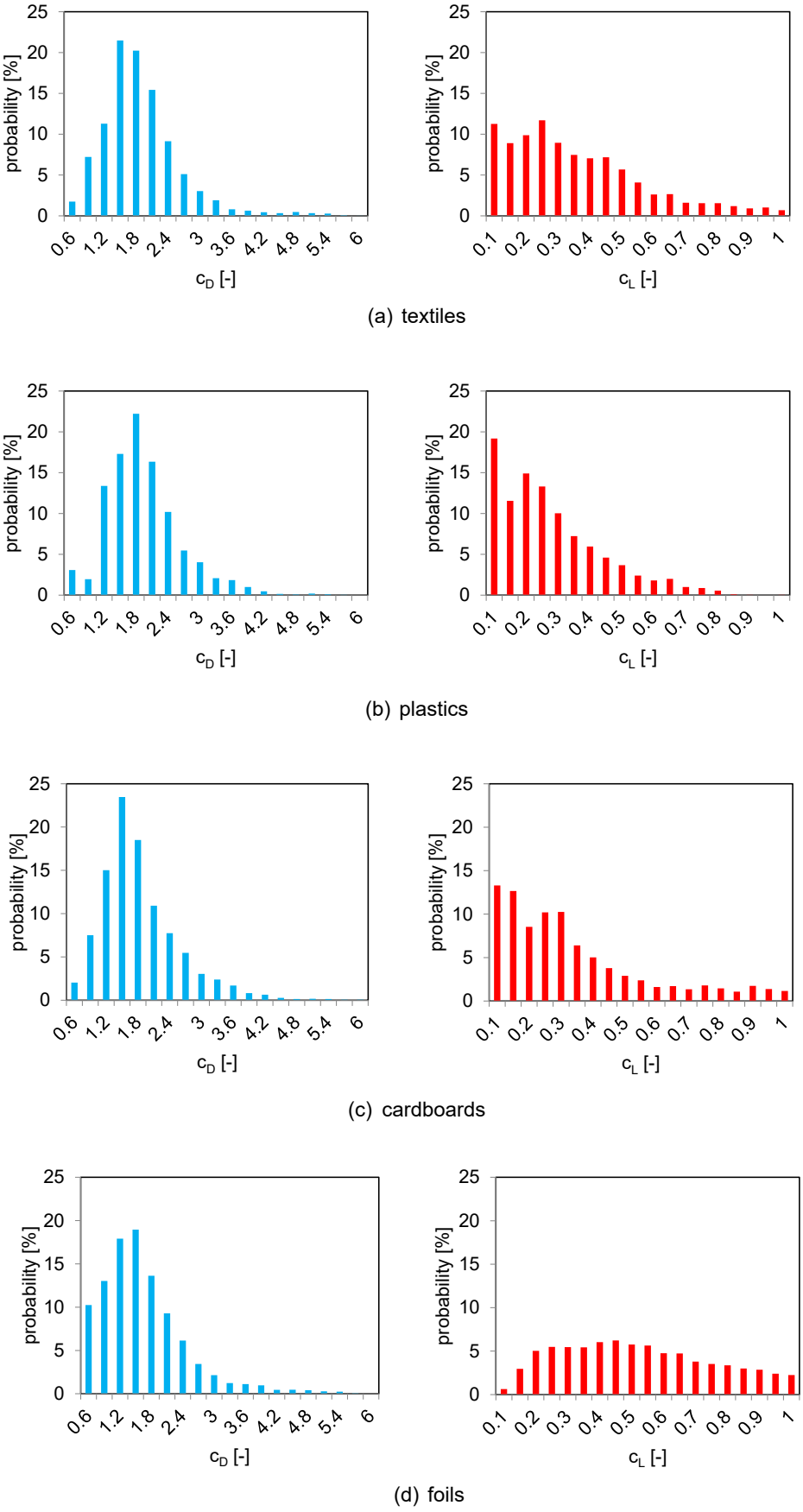

Fig. 17. Frequency distribution of drag and lift coefficients for the FLUFF fractions considered.

Acknowledgment

This study was funded by the German Federation of Industrial Research Associations (AiF) on behalf of the German Federal Ministry for Economic Affairs and Climate Action (IGF-Project 20410N) and by the DFG (German Research Foundation) project number 215035359 TRR 129.

References

[1] Fischedick M, Görner K, Thomeczek M. CCS-Technologie: Speicherung und Nutzung von klimaschädlichem CO2. 1st ed. Berlin: Springer Berlin; 2013.
[2] Fachgebiet 3, "Dekarbonisierung der Zementindustrie," Dessau-Roßlau, Feb. 2022. Accessed: Nov. 12 2022. [Online]. Available: https://www.umweltbundesamt.de/sites/default/files/medien/376/dokumente/factsheet_zementindustrie.pdf.
[3] Liedmann B, et al. An approach to model the thermal conversion and flight behaviour of Refuse Derived Fuel. Fuel 2017;200:252–71. https://doi.org/10.1016/j.fuel.2017.03.069.
[4] Krueger B, Wirtz S, Scherer V. Measurement of drag coefficients of non-spherical particles with a camera-based method. Powder Technol 2015;278:157–70. https://doi.org/10.1016/j.powtec.2015.03.024.
[5] B. Krueger, "Experimentelle Charakterisierung und Modellierung der Flugbewegung von asphärischen Partikeln," Dissertation, Karl-Maria Laufen Nachf. Wilhelm R. Kurze, Oberhausen.
[6] Pieper C, Liedmann B, Wirtz S, Scherer V, Bodendiek N, Schaefer S. Interaction of the combustion of refuse derived fuel with the clinker bed in rotary cement kilns: A numerical study. Fuel 2020;266:117048. https://doi.org/10.1016/j.fuel.2020.117048.
[7] Haider A, Levenspiel O. Drag coefficient and terminal velocity of spherical and nonspherical particles. Powder Technol 1989;58(1):63–70. https://doi.org/10.1016/0032-5910(89)80008-7.
[8] Ganser GH. A rational approach to drag prediction of spherical and nonspherical particles. Powder Technol 1993;77(2):143–52. https://doi.org/10.1016/0032-5910(93)80051-B.
[9] Hölzer A, Sommerfeld M. New simple correlation formula for the drag coefficient of non-spherical particles. Powder Technol 2008;184(3):361–5. https://doi.org/10.1016/j.powtec.2007.08.021.
[10] Song X, Xu Z, Li G, Pang Z, Zhu Z. A new model for predicting drag coefficient and settling velocity of spherical and non-spherical particle in Newtonian fluid. Powder Technol 2017;321:242–50. https://doi.org/10.1016/j.powtec.2017.08.017.
[11] Nakhaei M, et al. Aerodynamic and Physical Characterization of Refuse Derived Fuel. Energy Fuels 2018;32(7):7685–700. https://doi.org/10.1021/acs.energyfuels.8b01359.
[12] B. Liedmann, "Simulation der thermischen Umsetzung flugfähiger Ersatzbrennstoffe in Drehrohröfen der Zementindustrie," Dissertation, Ruhr-Universität Bochum, Aachen.
[13] Korte T. Evaluierung von möglichen Verfahren zur diskreten Abbildung grobstückiger Brennstoffe in DEM-Simulationen. Bachelorthesis: Department of Energy Plant Technology, Ruhr University Bochum, Bochum; 2019.
[14] David G. Lowe, *Object Recognition from Local Scale-Invariant Features*, 2001. [Online]. Available: https://www.researchgate.net/publication/2373439_Object_Recognition_from_Local_Scale-Invariant_Features.
[15] Zhang Z. A flexible new technique for camera calibration. IEEE Trans Pattern Anal Machine Intell 2000;22(11):1330–4. https://doi.org/10.1109/34.888718.
[16] J. L. Schonberger and J.-M. Frahm, "Structure-from-Motion Revisited," in *2016 IEEE Conference on Computer Vision and Pattern Recognition (CVPR 2016): Las Vegas, Nevada, USA, 27-30 June 2016*, Las Vegas, NV, USA, 2016, pp. 4104–4113.
[17] M. Kazhdan and H. Hugues, "Screened poisson surface reconstruction," in *ACM Transactions on Graphics,*, pp. 1–13. [Online]. Available: 10.1145/2487228.2487237.
[18] Bernardini F, Mittleman J, Rushmeier H, Silva C, Taubin G. The ball-pivoting algorithm for surface reconstruction. IEEE Trans Vis Comput Graph 1999;5(4):349–59. https://doi.org/10.1109/2945.817351.
[19] Mirtich B. Fast and Accurate Computation of Polyhedral Mass Properties. J Graphics Tools 1996;1(2):31–50. https://doi.org/10.1080/10867651.1996.10487458.
[20] D. Emeis, "Klassifizierung von EBS-Partikelorientierungen in einem Fallschacht mittels Image Processing und Computer Vision," Masterthesis, Department of Energy Plant Technology, Ruhr University Bochum, Bochum, 2021.
[21] Swinbank R, James Purser R. Fibonacci grids: A novel approach to global modelling. QJR Meteorol Soc 2006;132(619):1769–93. https://doi.org/10.1256/qj.05.227.
[22] D. Modrow, "Echtzeitfähige aktive Stereoskopie für technische und biometrische Anwendungen," Dissertation, Fakultät für Elektrotechnik und Informationstechnik, Technical University of Munich, Munich, 2008. Accessed: Nov. 12 2022. [Online]. Available: https://mediatum.ub.tum.de/doc/653321/653321.pdf.
[23] Szeliski R. Computer Vision: Algorithms and Applications. London: Springer London; 2011.
[24] J. Horn, A. Bachmann, and T. Dang, "Stereo Vision Based Ego-Motion Estimation with Sensor Supported Subset Validation," in *2007 IEEE Intelligent Vehicles Symposium*, Istanbul, Turkey, 2007, pp. 741–748.
[25] R. Hartley and A. Zisserman, *Multiple view geometry in computer vision*. Cambridge: Cambridge University Press, 2003 [reimpr. 2008.
[26] A. Fusiello, "Tutorial on Rectification of Stereo Images," Department of mathematics and informatics, Udine, 1999. Accessed: Nov. 12 2022. [Online]. Available: https://www.researchgate.net/publication/2841773_Tutorial_on_Rectification_of_Stereo_Images/link/0c9605278c3c136798000000/download.
[27] Z. Huang and J. Leng, "Analysis of Hu's moment invariants on image scaling and rotation," in *ICCET 2010: 2010 International Conference on Computer Engineering and Technology : 16-18 April, 2010, Chengdu, China : proceedings*, Chengdu, China, 2010, V7-476-V7-480.
[28] Steger C. A Comprehensive and Versatile Camera Model for Cameras with Tilt Lenses. Int J Comput Vis 2017;123(2):121–59. https://doi.org/10.1007/s11263-016-0964-8.
[29] Hu M-K. Visual pattern recognition by moment invariants. IEEE Trans Inform Theory 1962;8(2):179–87. https://doi.org/10.1109/TIT.1962.1057692.
[30] S. Sutiworwan, M. Ruchanurucks, P. Apiroop, S. Siddhichai, T. Chanwimaluang, and M. Sato, "Planar surface area calculation using camera and orientation sensor," in *2012 IEEE International Conference on Cyber Technology in Automation, Control, and Intelligent Systems*, Bangkok, May. 2012 - May. 2012, pp. 377–381.
[31] Fahrmeir L, Heumann C, Künstler R, Pigeot I, Tutz G. Statistik: Der Weg zur Datenanalyse [Online]. Available:. 8th ed. Berlin, Heidelberg: Springer Spektrum; 2016.
[32] Hoerner SF. Fluid-dynamic drag: Practical information on aerodynamic drag and hydrodynamic resistance. 2nd ed. Bakersfield: Hoerner Fluid Dynamics; 1992 (1965)..
[33] Baker WE. Explosion hazards and evaluation [Online]. Available: Amsterdam a.o: Elsevier; 1983.
[34] Aaronaes AS, Nilsson H. Dynamic response of pipe rack steel structures to explosion loads. Accessed: Nov. 21 2022. [Online]. Available:. Masterthesis, Division of Structural Engineering. Chalmers University of Technology, Göteborg; 2014.
[35] Zhou S, Zhang G, Xu X. Experiments on the Drag and Lift Coefficients of a Spinning Sphere. Water 2022;14(17):2593. https://doi.org/10.3390/w14172593.